An optoelectronic band-to-band tunnel transistor for near-infrared sensing applications: Device physics, modeling, and simulation

Partha Sarathi Gupta, Hafizur Rahaman', Kunal Sinha, and Sanatan Chattopadhyay

Citation: J. Appl. Phys. **120**, 084510 (2016); doi: 10.1063/1.4961426
View online: http://dx.doi.org/10.1063/1.4961426
View Table of Contents: http://aip.scitation.org/toc/jap/120/8
Published by the American Institute of Physics

An optoelectronic band-to-band tunnel transistor for near-infrared sensing applications: Device physics, modeling, and simulation

Partha Sarathi Gupta,[1] Hafizur Rahaman,[1,a)] Kunal Sinha,[1] and Sanatan Chattopadhyay[2]
[1]*School of VLSI Technology, Indian Institute of Engineering Science and Technology, Shibpur 711103, India*
[2]*Department of Electronics Science, Calcutta University, Kolkata 700009, India*

(Received 24 May 2016; accepted 8 August 2016; published online 30 August 2016)

In this article, we propose a novel optoelectronic band-to-band tunnel field effect transistor with a Si photo-gate, for multi-spectral sensing of near-infrared light in the wavelength range of 0.7 μm–1 μm. Based on the line tunneling approach, a drain current model has been developed to illustrate the device operating principle. The model incorporates the effect of photo-generation in the photo-gate in terms of the resulting photo-voltage. Good agreement with device simulation results indicates overall correctness of the developed model. The spectral response of the device has been studied in terms of its input and output characteristics, and the spectral sensitivity has been defined in terms of the change in current, in response to the change in the illumination wavelength. The proposed device can resolute closely spaced spectral lines ($\sim$100 nm) in the wavelength range of 0.7 μm–1 μm, due to the combined effects of steep average sub-threshold swing of $\sim$19 mV/dec, over five current decades, and current modulation due to change in the tunnel path length, induced by the gating effect of the photo-generated carriers. Peak spectral sensitivity at an illumination intensity of 0.5 W/cm^{-2} is found to be 5.88×10^3, 2.14×10^3, and 3.56×10^2 corresponding to decrease in illumination wavelength from (1 μm to 0.9 μm), (0.9 μm to 0.8 μm), and (0.8 μm to 0.7 μm), respectively. The influence of different device parameters, on the spectral sensing performance of the device, is thoroughly investigated by TCAD simulations and through the developed model. *Published by AIP Publishing*. [http://dx.doi.org/10.1063/1.4961426]

I. INTRODUCTION

Near infrared sensing and imaging finds multitude applications in defense, home-land security, and life sciences.[1,2] Near-infrared light in the wavelength range of 700 nm to 1.4 μm is particularly useful for molecular detection due to greater tissue penetrability and lesser photo-damage to biomolecules in this energy range.[3] Such detection requires the photo-detector to provide spectral differentiation among a discrete set of well separated wavelengths ($\sim$100 nm) at low intensity of illumination (e.g., $<$1 W/cm^{-2}).[4] Metal-oxide-semiconductor field effect transistors (MOSFETs) have been studied theoretically and experimentally for various optically controlled applications.[5,6] Potential of these devices for their use as photo-detectors is extended by the advantages, such devices provide in terms of integrated circuit compatibility, low voltage operation, and superior noise performance in comparison to avalanche photodiodes. When the condition of separation of absorbing and conducting regions is achieved in such devices, by suitable choice of gate and channel materials, modulation in current is caused by the gating effect of the photo-generated carriers in the gate.[7] For sensing closely spaced spectral lines, at low intensity of illumination, the FET sensors are required to exhibit current modulation in response to the change in the gating effect induced by change in illumination wavelength. The sub-threshold regime constitutes the optimal sensing domain for any FET based sensor. The sub-threshold swing (*SS*) of any FET is a critical parameter, which provides an indication of the efficiency of the gating effect, and thus it controls the sensitivity of the device. Conventional FETs are unable to exhibit multi-spectral sensitivity in the sub-threshold regime because the minimum achievable *SS* for such devices is fundamentally limited to 60 mV/dec at room temperature.[8] In contrast, tunnel FETs (TFETs) can achieve sub-Boltzmann switching due to carrier injection through the band-to-band tunneling (BTBT) mechanism.[9,10] Such attributes make TFETs promising candidate not only for low standby power (LSTP) applications[11] but also for bio-sensing[12] and light sensing applications.[13,14]

This work focuses on the design and modeling of a novel photosensitive band-to-band TFET, for multi-spectral sensing of near-infrared light, in the wavelength (λ) range of 700 nm–1 μm. A relevant transport model, based on the line tunneling viewpoint of TFET device operation,[15] has been developed to explain its operating principle. The accuracy of the model is tested by comparing the results obtained from the model with those obtained from 2-D numerical simulations using a commercial TCAD simulator S-Device.[16] The spectral response of the device has been studied in terms of its input and output characteristics. To provide the design direction of the proposed device, the influence of different device parameters, on the spectral sensing performance of the device, is discussed and studied in detail by TCAD simulations and through the developed model.

II. DEVICE STRUCTURE AND OPERATING PRINCIPLE

Fig. 1(a) shows the schematic of the proposed device structure. The device considered in this work is a Si/Ge

a)Electonic mail: hafizur@vlsi.iiests.ac.in

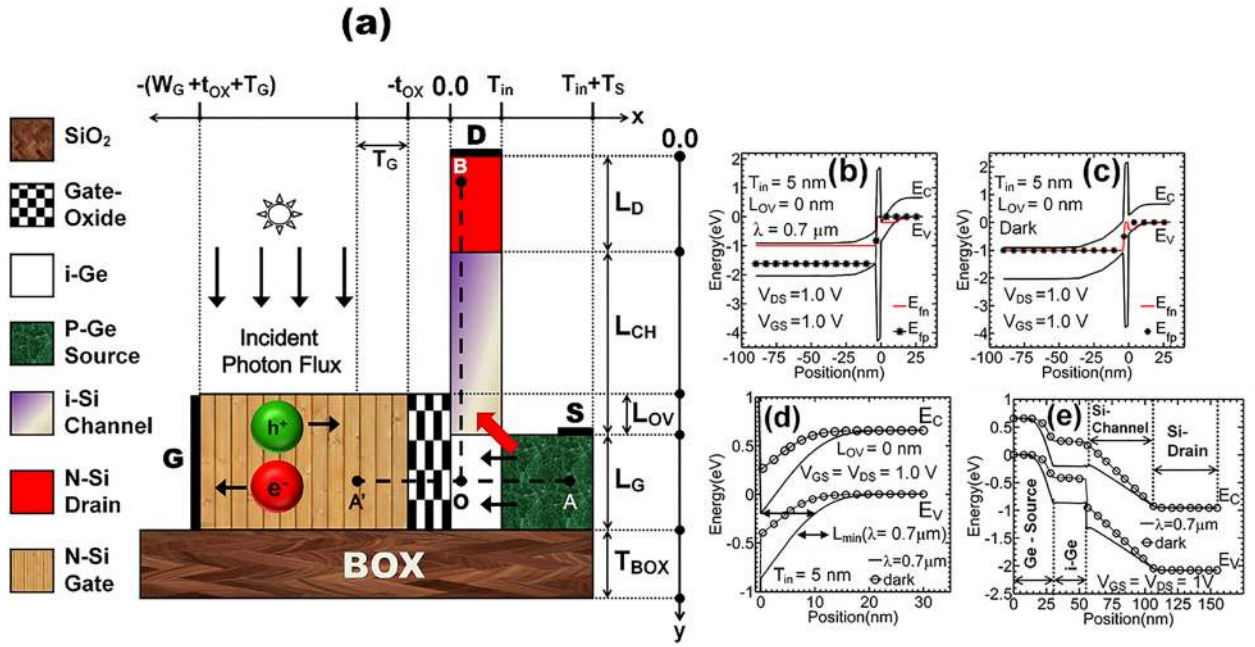

FIG. 1. (a) Schematic of the proposed device structure. Carrier transitions from the valence band of the p-Ge region to the conduction band of the i-Ge region along the gate electric field are indicated by black arrows. Red arrows indicate diagonal tunneling. (b) ON state ($V_{GS} = V_{DS} = 1$ V) energy band diagram obtained at the illuminated condition ($I_0 = 0.5$ W/cm^2, $\lambda = 0.7\,\mu$m) along the cutline $A'A$, illustrating the separation of electron(hole) quasi Fermi energy levels, E_{fn} (E_{fp}) in the gate region due to photo-generation in that region. (c) Corresponding energy band diagram obtained at the dark condition. E_{fn} and E_{fp} coincide in the gate region at the dark condition. (d) Comparative ON state energy band diagram, along the cutline OA, obtained at dark and illuminated conditions. Minimum tunnel path length at the illuminated condition, L_{min} ($\lambda = 0.7\,\mu$m), is indicated. (e) Corresponding energy band profile along the current transport direction, i.e., along the cutline AO and OB. T_{in} and L_{OV} are chosen to be 5 nm and 0 nm.

hetero-structure n-type TFET. It comprises a side-trench n-type Si photon absorbing gate, an intrinsic Si (i-Si) channel region, a n-type Si drain region, and a Ge source having a retrograde doping profile, obtained by the incorporation of an intrinsic Ge region. The device is specifically a band-to-band tunnel FET, involving carrier transition from the valence band of the p-type region of the Ge source (p-Ge) to the conduction band of the intrinsic region of the Ge source (i-Ge) and to the conduction band of the i-Si channel region. The high-k gate-oxide thickness has been supposed to be t_{OX} nm, and the buried-oxide (BOX) thickness is chosen to be T_{BOX} μm. The thickness of the i-Si channel region, i-Ge region, and n-type Si drain region is each assumed to be T_{in} nm. The thickness of the p-Ge region has been taken to be T_S nm. The gate-to-source overlap length, gate-to-channel overlap length, length of i-Si channel region, and length of the drain region have been supposed to be L_G nm, L_{OV} nm, L_{CH} nm, and L_D nm, respectively. The doping concentration in the source, drain, and gate are supposed to be N_A cm^{-3}, N_D cm^{-3}, and N_G cm^{-3}, respectively. The illumination window of the photo-gate spans from $-(W_G + t_{OX} + T_G) < x < -T_G$, and the gate region is assumed to be $(W_G + T_G)$ μm wide. The structural parameters used in this work are summarized in Table I. At the illuminated condition, under normal incidence on the illumination window, excess electron-hole pairs (EHPs) are generated in the gate region. Photogeneration in the gate region occurs due to absorption of incident photons having energies in excess of the band-gap energy of Si. Movement of the photo-generated carriers within the gate region is governed by the combined effects of the applied gate bias (V_{GS}) and band bending in the gate. When V_{GS} is positive, photo-generated electrons move towards the gate electrode, while the excess holes accumulate near the gate/gate-oxide interface. Such charge separation perturbs the equilibrium condition in the gate. Consequently, the electron quasi-Fermi energy (E_{fn}) and the hole quasi-Fermi energy (E_{fp}) get separated in the gate region leading to the development of net photo-voltage (V_{OP}) across it. Such separation of E_{fn} and E_{fp} in the gate region is illustrated in the ON state ($V_{GS} = V_{DS} = 1$ V) energy band diagram shown in Fig. 1(b), obtained along the cut-line $A'A$, through the center of the gate-to-source overlap region, at the illuminated condition ($\lambda = 0.7\,\mu$m). However, E_{fn} and E_{fp} coincide at the dark

TABLE I. Device structural parameters used in simulation and modeling.

Parameters	Value
Length of illumination window of the gate (W_G)	1.0 μm
Length of the gate region ($W_G + T_G$)	1.01 μm
Gate-to-source overlap length (L_G)	50 nm
Channel length (L_{CH})	50 nm
Length of the drain region (L_D)	50 nm
Gate-to-channel overlap length (L_{OV})	0 nm–20 nm
Gate-oxide thickness (t_{OX})	4 nm
Dielectric constant of gate-oxide	22
Buried oxide (BOX) thickness (T_{BOX})	1.0 μm
Thickness of the i-Ge region, channel region, and drain region (T_{in})	5 nm–10 nm
Thickness of the p-Ge region of the source (T_S)	25 nm
Acceptor doping concentration in the p-Ge region (N_A cm^{-3})	5×10^{18}
Donor doping concentration in the drain region (N_D cm^{-3})	5×10^{18}
Donor doping concentration in the gate region (N_G cm^{-3})	1×10^{18}

condition, as shown in Fig. 1(c), confirming that the equilibrium condition prevails in the gate region at the dark condition. The photo-voltage acts as an additional gate bias which lowers the onset gate voltage or the turn ON voltage (V_{ONSET}) required for the alignment of filled valence band density of states (DOS) in the p-Ge region with the empty conduction band DOS in the i-Ge region and i-Si channel region. Consequently, BTBT current increases. Comparative ON state energy band plots, obtained along the cut-line *OA*, through the center of the gate-to-source overlap region, at illuminated ($\lambda = 0.7\ \mu$m) and dark conditions are shown in Fig. 1(d). The overlap between the conduction band and valence band DOS is observed only at the illuminated condition ($\lambda = 0.7\ \mu$m), and the relevant minimum tunnel path length, L_{min} ($\lambda = 0.7\ \mu$m), is indicated in Fig. 1(d). The corresponding band diagram along the current transport direction, i.e., along *AOB*, is shown in Fig. 1(e). The illumination window is chosen such that photo-generation primarily occurs in the gate region. Therefore, its contribution to the OFF state leakage current (I_{OFF}) is negligible, and I_{OFF} is determined by the reverse biased source-to-drain diode leakage current. The low band gap of Ge used in the source leads to higher ON state current (I_{ON}) due to high BTBT offered by Ge. The total BTBT current can be divided into two components: (1) The BTBT current component due to carrier transition from the valence band of the p-Ge region to the conduction band of the i-Ge region. The tunneling direction in this case is perpendicular to the gate-oxide/i-Ge interface. This type of tunneling is called the "gate-normal tunneling"[17] or more generally "line tunneling."[15] (2) The BTBT current component due to carrier transition from the valence band of the p-Ge region to the conduction band of the i-Si channel region. The tunneling direction in this case is not perpendicular to the gate-oxide/i-Ge interface. This type of tunneling is called the diagonal tunneling.[17] To achieve high spectral sensitivity, low *SS* is required. Steep switching slopes can be achieved by designing the structure such that the line tunneling component dominates over the diagonal tunneling component in the subthreshold regime of device operation. The turn ON voltage for line tunneling (V_{ONSET}^{line}) and diagonal tunneling ($V_{ONSET}^{diagonal}$) components of BTBT current in such a structure is different. The line tunneling component of BTBT current is controlled by the gate-to-source overlap length, while the gate-to-channel overlap length controls the diagonal tunneling component of BTBT current. Therefore, L_G and L_{OV} are suitably chosen to target steep *SS* and reasonably high I_{ON}. The retrograde doping profile used in the source minimizes the process induced variation[18] and field induced quantum confinement (FIQC) effects.[19] The source doping level and T_{in} determine V_{ONSET}^{line}. Therefore, N_A and T_{in} must be chosen to maximize line tunneling and minimize *SS* for sub-volt operation at the illuminated condition. The p-Ge region is chosen to be adequately thick to support line tunneling. The drain doping concentration has been chosen to minimize BTBT at the channel/drain junction which increases the undesirable ambipolar conduction current prior to the onset of tunneling. Moderate doping has been used in the gate region to ensure high V_{OP} and high minority carrier life-time that leads to improvement in spectral sensitivity. The i-Si channel region is left undoped to reduce mobility degradation from Columbic scattering by ionized impurities and to eliminate the impact of dopant fluctuation on the device performance.

III. MODEL FORMULATION

The drain current model presented in this work is centered on the line tunneling view point of the TFET device operation.[15] Fig. 2 shows the energy band diagram schematic, illustrating the electrostatics and key parameters used in the model derivation. The key steps of the model are summarized as follows: (1) Expression for V_{OP} is developed in terms of the electron quasi-Fermi potential (ϕ_n) and the hole quasi-Fermi potential (ϕ_p) in the gate region, assuming the Shockley-Read-Hall (SRH) recombination mechanism to be the dominant recombination process for the photo-generated EHPs in the gate region. (2) 1-D Poisson's equation is solved in the gate region, i-Ge region and p-Ge region, along the cut-line $A'A$ (x-direction) to estimate the surface potential (Ψ_S) at the gate-oxide/i-Ge interface in terms of terminal voltages and V_{OP}. Uniform band bending is assumed at the gate-oxide/i-Ge interface throughout the gate-to-source overlap region. (3) Assuming carrier transition from the valence band of the p-Ge region to the conduction band of the i-Ge region, analytical expression for the minimum tunnel path length (L_{min}) is obtained in terms of Ψ_S. Carrier transitions from the valence band of the p-Ge region to the conduction band of the i-Si channel region are not considered. (4) Analytical expression for the overlap in position between filled valence band DOS in the p-Ge region with the empty conduction band DOS in the i-Ge region, X_{OV} (Ψ_S), is subsequently derived in terms of Ψ_S. Such overlap is indicated by the shaded region in the model band diagram schematic shown in Fig. 2. (5) Kane's model[20] is used to calculate the BTBT generation rate (G_{BTBT}). This model requires the average field over a tunneling path to estimate the BTBT rate. However, there can be several tunneling paths contained in the overlap region of different lengths, each having different average electric field. Drain current is predominantly determined by the BTBT generation along the shortest tunnel path. Therefore, average electric field across the shortest tunneling path (ξ_{avg}) is estimated to calculate G_{BTBT}.

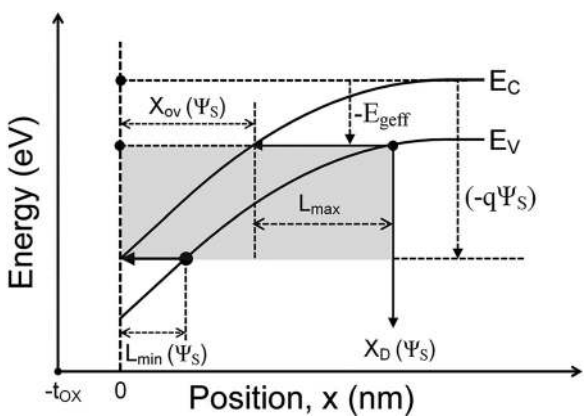

FIG. 2. Energy band diagram schematic for illustrating the electrostatics and key parameters used in the derivation.

(6) Assumption of uniform Ψ_S, throughout the gate-to-source overlap region, implies uniformity of V_{ONSET} across that region. In actuality, segments of the gate-to-source overlap region near to the i-Ge/i-Si channel metallurgical junction turn ON at lower V_{GS}, compared to the segments that are away from the junction. For correct estimation of the BTBT current at the onset of tunneling, an empirical bias dependent source doping concentration (N_S) is introduced. (7) Quantities such as $L_{min}(\Psi_S)$, ξ_{avg}, and G_{BTBT} are recomputed using N_S. Finally, the BTBT current is calculated from the recomputed BTBT rate by assuming it to be the main generation mechanism.

A. Expression for Photo-voltage (V_{OP})

Photo-generation in the gate region modifies electron and hole concentrations in that region. The quasi-equilibrium electron and hole concentrations in the gate region are, respectively, given by: $(n^* = n_0 + \Delta N(\lambda))$ and $(p^* = p_0 + \Delta N(\lambda))$, where n_0 and p_0 are the equilibrium electron and hole concentrations in the gate region at the dark condition and $\Delta N(\lambda)$ is the concentration of the EHPs generated in the gate region at an illumination wavelength (λ). Assuming SRH recombination to be the key recombination mechanism for the EHPs in the gate region, expression for $\Delta N(\lambda)$ can be written in the steady state as[21]

$$\Delta N(\lambda) = I_0 \alpha(\lambda) \tau \frac{\lambda}{hc}(1 - R_1)(1 - R_2), \tag{1}$$

where I_0 is the illumination intensity, $\alpha(\lambda)$ is the absorption coefficient per unit length of the gate region at the energy of incident photons, h is the Planck's constant, c is the velocity of light, and τ is the carrier life time. The reflection coefficient at the air-gate interface (R_1) and gate-BOX interface (R_2) are calculated as.[21] At illuminated conditions, the product of n^* and p^* can be written in terms of ϕ_n and ϕ_p in the gate region as

$$n^* p^* = n_i^2 \exp\left(\frac{\phi_p - \phi_n}{U_T}\right), \tag{2}$$

where n_i is the intrinsic carrier concentration of the gate material and U_T is the thermal potential. The photon induced shift in the gate voltage is approximately given by $(\phi_p - \phi_n)$. Thus, V_{OP} can be written as

$$V_{OP} = U_T \ln\left[1 + \left(\frac{\Delta N}{n_i}\right)^2 + \frac{\Delta N}{N_G}\left(1 + \exp\left(-\frac{2\phi_{FG}}{U_T}\right)\right)\right], \tag{3}$$

where ϕ_{FG} is the gate Fermi potential at equilibrium. It may be noted that under low level injection approximation, this formula predicts the correct slope of V_{OP} versus illumination intensity, viz., U_T.[22]

B. Surface Potential Computation

Assuming uniform doping in the gate region, solution to 1-D Poisson's equation in that region along the cutline $A'A$, through the center of the gate-to-source overlap region, yields the total gate charge (Q_G) in terms of the electrostatic potential (Ψ_P) at the gate/gate-oxide interface.

$$Q_G = \sqrt{2q\varepsilon_{Si}N_G}\sqrt{\psi_P + U_T\left(\exp\left(-\frac{\psi_P}{U_T}\right) - 1\right) + \exp\left(\frac{-\phi_{FG}}{U_T}\right)\left(U_T \exp\left(\frac{\psi_P}{U_T}\right) - \psi_P - U_T\right)}, \tag{4}$$

where ε_{Si} is the permittivity of Si and q is the electronic charge. Assuming uniform doping in the p-Ge region with an abrupt interface between i-Ge and p-Ge regions, the total semiconductor charge (Q_S) can be found in terms of Ψ_S by solving 1-D Poisson's equation along the cut-line $A'A$ in the i-Ge region and p-Ge region, following a similar methodology reported in Ref. 23

$$Q_S = -\sqrt{2q\varepsilon_{Ge}N_A}\sqrt{\psi_S - 2\sqrt{\beta}\sqrt{\psi_B - U_T} + U_T\left(\exp\left\{\frac{\psi_S - 2\phi_F - \phi_{Fn}}{U_T}\right\} - 1\right)}, \tag{5a}$$

where ε_{Ge} is the permittivity of Ge, Ψ_B is the electrostatic potential at the i-Ge region and the p-Ge region interface, ϕ_F is the Fermi potential in the p-Ge region of the source, and ϕ_{Fn} is the electron quasi-Fermi potential in the source region relative to ϕ_F. The drain bias (V_{DS}) influences Q_S by increasing ϕ_{Fn} relative to ϕ_F. In this model, ϕ_{Fn} is assumed to be equal to V_{DS} up to the source depletion region edge. Such assumption is valid only in the tunneling limited regime of device operation, where the current levels are low. In Eq. 5(a), Ψ_B and Ψ_S are related as[23]

$$\psi_B = U_T + (\sqrt{\psi_S - U_T + \beta} - \sqrt{\beta})^2, \tag{5b}$$

where $\beta = \frac{qN_A}{2\varepsilon_{Ge}}T_{in}^2$. Using Eq. 5(b) in Eq. 5(a), expression for the source depletion charge (Q_B) can be obtained as: $Q_B = -\sqrt{2q\varepsilon_{Ge}N_A}\sqrt{\psi_B - U_T}$. The potential balance equation, incorporating the effect of photo-generation in the gate region, can be written as

$$V_{GS} - V_{FB} + V_{OP} = \psi_S + \psi_P - \frac{Q_S}{C_{OX}}, \tag{6a}$$

where V_{FB} is the flat-band voltage and $C_{OX} = \varepsilon_{OX}/t_{OX}$ is the gate-oxide capacitance per unit area, where ε_{OX} is the permittivity of gate-oxide. The gate insulator has been assumed to be free from any charges. Under such assumption, total gate charge must balance the net semiconductor charge. Thus, the charge balance equation can be written as

$$Q_G + Q_S = 0. \tag{6b}$$

The potential and charge balance equations can be solved numerically to obtain Ψ_S in terms of terminal voltages and V_{OP}.

C. Drain Current Computation

Estimation of minimum tunnel path length requires the potential profile in the i-Ge region and the p-Ge region. The potential variation in the i-Ge region along the x-direction, $\Psi_1(x)$, has been assumed to be linear because this region is undoped. The potential variation in the p-Ge region along the x-direction, $\Psi_2(x)$, has been assumed to be parabolic. Such assumption is fairly valid when the inversion charge density is small. These assumptions are necessary to obtain an analytical expression for L_{min} (Ψ_S). The potential variation $\Psi_1(x)$ and $\Psi_2(x)$ can be written as: $\psi_1(x) = \frac{\psi_B - \psi_S}{T_{in}} x + \psi_S$ and $\psi_2(x) = \psi_B \left(\frac{X_D(\psi_S) - x}{X_D(\psi_S) - T_{in}}\right)^2$, where $X_D(\psi_S) = \sqrt{\frac{2\varepsilon_{Ge}}{qN_A}\psi_S + T_{in}^2}$ is the total depletion width in the source region. Analytical expression for $L_{min}(\Psi_S)$ can be found by equating x-coordinates of points of equal energy in the valence band of the p-Ge region and the conduction band of the i-Ge region.[15]

$$L_{\min}(\psi_S) = X_D(\psi_S) - (X_D(\psi_S) - T_{in})\sqrt{\frac{\psi_S}{\psi_B} - \frac{E_{geff}}{q\psi_B}}, \tag{7}$$

where E_{geff} is the effective band-gap of Ge extracted from simulated band profile incorporating band-gap narrowing effects. Expression for the maximum tunnel path length (L_{max}) can be obtained by substituting E_{geff} for Ψ_S in Eq. (7). The overlap (in position) between the filled valence band DOS in the p-Ge region with the empty conduction band DOS in the i-Ge region can be estimated from $\Psi_1(x)$ as: $X_{OV}(\psi_S) = \frac{\psi_S - E_{geff}}{\psi_S - \psi_B} T_{in}$. BTBT generation due to such overlap can be estimated using Kane's model.[20] In the uniform electric field limit, the model can be written in a manner similar to the non-local BTBT model used in the simulation tool.[16]

$$G_{BTBT} = A\left(\frac{\xi_{avg}}{F_0}\right)^D \exp\left(-\frac{B}{\xi_{avg}}\right)(f_{pS} - f_{nS}), \tag{8}$$

where A and B are material dependent constants of the model, $F_0 = 1$ V/cm, and the parameter D distinguishes between the direct ($D = 2$) and the indirect ($D = 2.5$) tunneling process, and f_{pS} and f_{nS} are the Fermi distribution functions in the source region corresponding to ϕ_F and ϕ_{Fn}, respectively. It may be noted that the inclusion of the term $(f_{pS} - f_{nS})$ ensures zero generation at the equilibrium condition. Average electric field along the shortest tunnel path has been estimated as: $\xi_{avg} = \frac{E_{geff}}{qL_{\min}(\psi_S)}$. The electrostatic model developed thus far assumes invariance of Ψ_S along the y-direction (parallel to the gate-oxide/i-Ge interface). Such assumption implies that the entire source region has a single turn ON voltage. Fig. 3 plots the simulated electron BTBT generation rate profile in the gate-to-source overlap region, obtained along a cut-line parallel to the gate-oxide/i-Ge interface at a distance of 0.5 nm from it. Plots are obtained at the illuminated condition ($\lambda = 0.7$ μm) with V_{DS} fixed at 1 V for different V_{GS} values. It can be observed that, at relatively low V_{GS}, electron BTBT generation is confined near the i-Ge/i-Si channel metallurgical junction. As V_{GS} is gradually increased, portions of the source region, away from the i-Ge/i-Si channel metallurgical junction, gradually turn ON and contribute to the BTBT current. For relatively large values of V_{GS}, BTBT generation is observed in the entire gate-to-source overlap region (along the y-direction). Thus, the turn ON voltage for the segments of the source region near to the i-Ge/i-Si channel metallurgical junction is lower compared to the segments that are away from the junction. The spatial variation in the turn ON voltage should be considered for correct estimation of BTBT current at the onset of tunneling. However, such consideration requires correct estimation of Ψ_S along the y-direction in the gate-to-source overlap region and corresponding computation of $G_{BTBT}(y)$. In order to obtain a closed form expression of drain current (I_{DS}), some simplifications are necessary. To address this issue, the source doping concentration has been considered to be a bias dependent quantity. In this regard, we introduce an empirical bias dependent source doping concentration, chosen as a linear function of the ratio of the electric field (ξ_{loc}) at the initial point ($x = L_{min}$) of the shortest tunneling path, and the surface electric field (ξ_S) at the i-Ge/gate-oxide interface

$$N_S(\psi_S) = N_{OFF} + \gamma\left(\frac{\xi_{loc}(\psi_S)}{\xi_S(\psi_S)}\right)N_A, \tag{9}$$

where N_{OFF} and γ are empirical fitting parameters. Under depletion approximation, the electric field varies linearly with position (x) in the p-Ge region and it maintains a constant value of ξ_S in the i-Ge region ($0 \le x \le T_{in}$). Thus, ξ_{loc} can be written in terms of ξ_S as: $\xi_{loc}(\psi_S) = \xi_S(\psi_S)\{1 - \frac{L_{\min}(\psi_S)}{X_D(\psi_S)}\}$, where ξ_S can be computed from Q_B using Gauss's

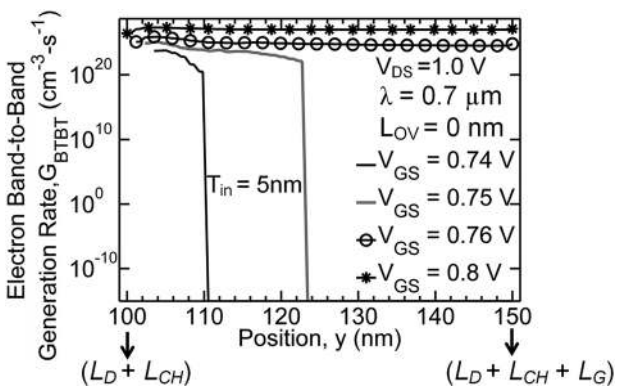

FIG. 3. Simulated electron BTBT generation rate profile in the gate-to-source overlap region, obtained along a cut-line parallel to the gate-oxide/i-Ge interface at a distance of 1 nm from it. Plots are obtained at the illuminated condition ($\lambda = 0.7$ μm) with V_{DS} fixed at 1 V for different V_{GS} values. T_{in} and L_{OV} are chosen to be 5 nm and 0 nm.

law. The source depletion region edge is the starting point of the tunneling path at the onset of vertical tunneling. Thus, at the onset of line tunneling, $\xi_{loc} = 0$ and N_S is determined by N_{OFF}. With increase in Ψ_S, $L_{min}(\Psi_S)$ decreases and the depletion width increases. Consequently, $N_S(\Psi_S)$ gradually increases with Ψ_S. The modified shortest tunnel path length ($L_{\min}^{new}$), computed by substituting N_S (Ψ_S) for N_A in Eq. (7) is thus larger in comparison to corresponding L_{min}, for Ψ_S values close to E_{geff}. Consequently, the average field (ξ_{AVG}^{new}) and the BTBT generation rate (G_{BTBT}^{new}), along the modified shortest tunnel path of length $L_{\min}^{new}$, are lower in comparison to the corresponding ξ_{avg} and G_{BTBT} along the shortest tunnel path of length L_{min}. As Ψ_S increases, $L_{\min}^{new}$ gradually approaches L_{min}. Thus, N_{OFF} and γ can be chosen appropriately to estimate the BTBT current at the onset of vertical tunneling and to match I_{ON}. Finally, drain current is calculated, assuming constant generation in the energy overlap region, as

$$I_{DS} = qW \int_0^{L_G} \int_0^{X_{OV}} G_{BTBT}^{new} dxdy \approx qWL_G X_{OV} G_{BTBT}^{new}, \quad (10)$$

where W is the width of the device along the z-direction.

IV. RESULTS AND DISCUSSIONS

Device performance has been studied by 2-D numerical simulations using a commercial TCAD simulator S-Device.[16] A dynamic non-local path BTBT model, capable of incorporating different tunneling directions and paths with slope of energy bands, has been used to emulate the BTBT behavior. For Si, the BTBT parameters provided in the simulation tool are used. These parameters are extracted from the experimental data of a p-n tunnel diode.[24] Experimentally calibrated BTBT parameters for Ge, reported in Ref. 25, have been used to obtain the simulation results. Fermi-Dirac statistics, band-gap narrowing model, and concentration and field dependent mobility models along with the Shockley-Read-Hall (SRH) recombination model are considered. Optical generation is computed using the ray tracer method through the effective band-gap dependent quantum yield model. Optical constants for Si are obtained from Ref. 26. Redistribution of carriers near the gate-oxide is included using the modified local-density approximation (MLDA) model. Such a model does not take into account the FIQC effects.[19] In the proposed device, the introduction of the i-Ge region and non-degenerate source doping greatly minifies the detrimental effects of FIQC, and thus, such effects can be neglected to the first order. Simulation results are obtained, assuming a doping smearing of 1.5 nm/dec at the p-Ge/i-Ge junction and the channel/drain junction. Such assumptions are reasonable, as with recently reported techniques such as Excimer Laser Annealing (ELA),[27] Plasma doping (PLAD),[28] and dopant profile-steepening implant (DPSI),[29] it is possible to achieve almost abrupt junctions. Illumination intensity (I_0) is assumed to be 0.5 W/cm^2, and the illumination wavelengths are chosen in the near-infrared range (0.7 μm–1 μm). Subthreshold swing has been extracted from the simulated and modeled input characteristics as: $SS = \left(\frac{d\log_{10} I_{DS}}{dV_{GS}}\right)^{-1}$, and the average subthreshold swing (SS_{AVG}) has been calculated as: $SS_{AVG} = \frac{V_T - V_{ONSET}}{\log_{10} I_T - \log_{10} I_{ONSET}}$, where V_T and V_{ONSET} are the gate voltages corresponding to current levels of $I_T = 0.1$ μA/μm and $I_{ONSET} = 1$ pA/μm, respectively. Spectral sensing performance of the device has been evaluated in terms of its spectral sensitivity (S_n) which is defined as the increase in I_{DS} corresponding to decrease in illumination wavelength from λ_2 to λ_1, normalized by I_{DS} values corresponding to illumination wavelength, λ_2

$$S_n = \frac{I_{DS}(\lambda_1)}{I_{DS}(\lambda_2)} - 1. \quad (11)$$

Non-ideal effects such as defect assisted tunneling are not been considered. Such effects cause deterioration to SS in the low current range. In this work, key parameters such as SS_{AVG} and S_n are computed considering relatively high I_{ONSET} of 1 pA/μm. Thus, at such current levels, effects of these non-idealities are less significant,[30] due to the dominance of BTBT current.

A. Spectral response of the device

Fig. 4(a) plots the simulated device transfer characteristics and compares it with those obtained from the model given by Eq. (10). The transfer characteristics are obtained at the illuminated condition for different values of λ, with V_{DS} fixed at 1 V. Corresponding $L_{min} - V_{GS}$ characteristics, obtained from Eq. (7), are shown in Fig. 4(b). T_{in} and L_{OV} are assumed to be 5 nm and 0 nm, respectively. The model empirical fitting parameter, N_{OFF}, has been chosen to be 1.5×10^{18} cm^{-3}, and the parameter γ has been varied from 0.82 to 1.05 corresponding to λ variation from 0.7 μm to 1 μm. Both the simulated and modeled transfer characteristics exhibit similar trends of increase in V_{ONSET} and decrease in I_{ON}, with increase in λ. V_{ONSET} extracted from the simulated transfer characteristic curves decreases from 0.81 V to 0.735 V and corresponding I_{ON} increases from 0.8 μA/μm to 2.14 μA/μm, for decrease in λ from 1 μm to 0.7 μm. Photogeneration in the gate region increases as λ decreases. Thus, V_{OP} given by Eq. (3) increases, which leads to the reduction in V_{ONSET}. Consequently, at a fixed gate bias, L_{min} decreases, as can be observed in Fig. 4(b). The increase in I_{ON} is attributed to such a decrease in L_{min}. It can be observed from Fig. 4(a) that the modeled transfer characteristic curves show delayed onset relative to corresponding simulated transfer characteristics. This is due to the assumption of uniform band bending at the i-Ge/gate-oxide interface throughout the gate-to-source overlap region. It has been illustrated in the preceding section that the turn ON voltage for the segments of the source region near to the i-Ge/i-Si channel metallurgical junction is lower compared to the segments that are away from the junction, owing to greater band bending at the i-Ge/gate-oxide interface in these regions. Hence, the simulated transfer characteristic curves exhibit lower V_{ONSET} compared to corresponding modeled transfer characteristics. However, it may be noted that the introduction of bias dependent source doping concentration leads to the correct estimation of current at the onset of tunneling and also in the ON state. Both the simulated and modeled transfer characteristics

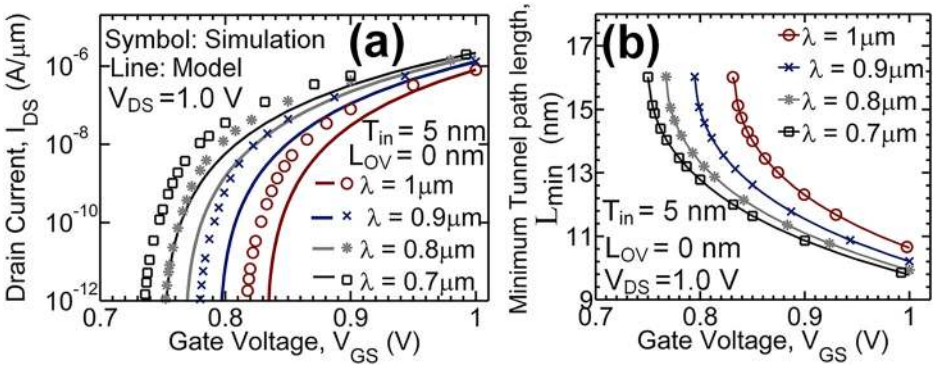

FIG. 4. (a) Comparative plots of simulated and modeled transfer characteristics, obtained at the illuminated condition for different values of λ, at $V_{DS} = 1$ V. (b) Corresponding L_{min}-V_{GS} characteristics. T_{in} and L_{OV} are assumed to be 5 nm and 0 nm, respectively.

exhibit very steep $SS_{AVG} \sim 19$ mV/dec and 21 mV/dec, respectively, in the wavelength range considered. Such steep SS_{AVG} is attributed mainly to the dominance of line tunneling. In the absence of any gate-to-channel overlap, band bending in the i-Si channel region in the vicinity of the i-Ge/i-Si metallurgical junction is controlled by gate fringing field. In such case, for the chosen value of T_{in} and N_A, diagonal tunneling is suppressed. Therefore, the total BTBT current is mainly determined by the line tunneling component. Fig. 5 plots the $S_n - I_{DS}$ characteristics corresponding to decrease in λ from (1 μm to 0.9 μm), (0.9 μm to 0.8 μm), and (0.8 μm to 0.7 μm), respectively. Spectral sensitivity has been computed from Eq. (11) using relevant pairs of transfer characteristic curves obtained from the simulation and model. It can be observed that S_n decreases at high current levels. This decrease is attributed to the gradual increase in SS when the device transits from tunneling limited regime to the transport limited regime with increase in V_{GS}. The peak value of spectral sensitivity (S_{nm}), extracted from the simulated ($S_n - I_{DS}$) characteristics, is found to be 5.88×10^3, 2.14×10^3, and 3.56×10^2 corresponding to decrease in λ from (1 μm to 0.9 μm), (0.9 μm to 0.8 μm), and (0.8 μm to 0.7 μm), respectively. Such high S_{nm} is a consequence of the steep SS_{AVG} owing to the dominance of line tunneling. Good agreement is observed between the $S_n - I_{DS}$ characteristics extracted from the modeled and simulated transfer characteristics. But, the model underestimates S_n in the current range of 1 pA/μm to 100 pA/μm. This is attributed to the greater SS_{AVG} exhibited by the modeled transfer characteristics compared to the corresponding simulated characteristics. It can be observed from Fig. 5 that, in the entire current range, S_n is

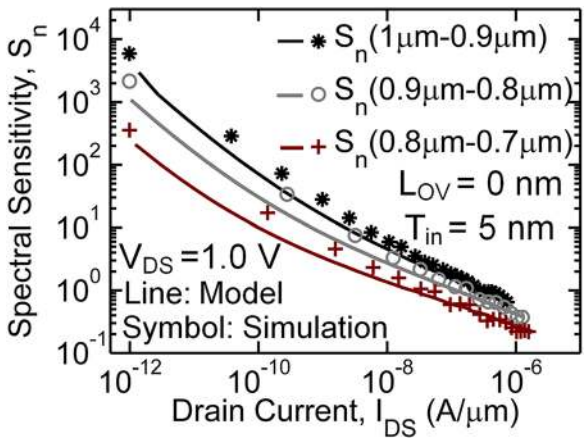

FIG. 5. Plots of variation of S_n with I_{DS} corresponding to decrease in λ from (1μm to 0.9 μm), (0.9 μm to 0.8 μm), and (0.8 μm to 0.7 μm), respectively. S_n values are computed using Eq. 11 using relevant pairs of transfer characteristic curves obtained from the simulation and model.

found to be highest for the wavelength pair (1 μm–0.9 μm). This is due to larger sensitivity of V_{OP} to wavelength changes in the low photon energy regime. It may be noted that S_n, for any wavelength pair, depends not only on the subthreshold swing of the relevant transfer characteristic curves but also on the separation of the I_{DS}–V_{GS} curves on the V_{GS} axis. The decrease in V_{ONSET} due to decrease in illumination wavelength is limited by the corresponding increase in V_{OP}. Consequently, S_n is also limited by such increase in V_{OP}. Comparative plots of output characteristics obtained from simulation and the model are shown in Fig. 6(a). Output characteristics are obtained at the illuminated

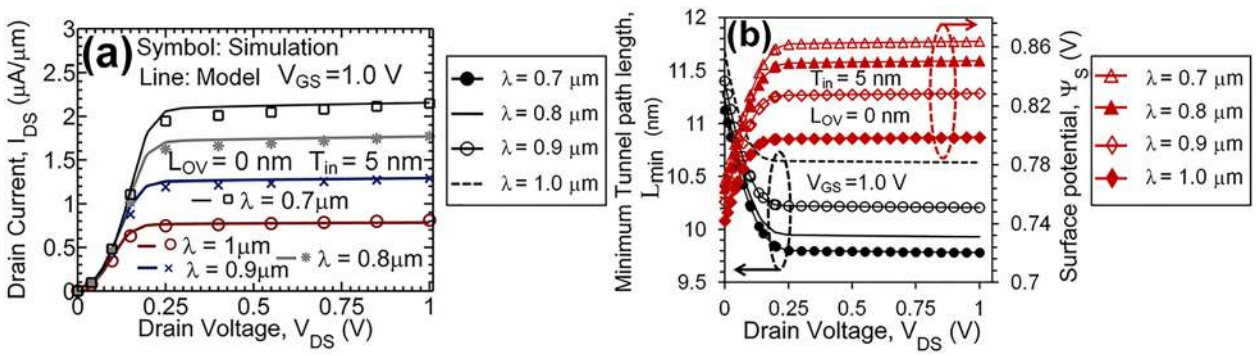

FIG. 6. (a) Comparative plots of output characteristics obtained from simulation and the model, obtained at the illuminated condition for different values of λ, at $V_{GS} = 1$ V. T_{in} and L_{OV} are assumed to be 5 nm and 0 nm, respectively. (b) Corresponding Ψ_S–V_{DS} and L_{min}–V_{DS} characteristics.

condition for different values of λ, with V_{GS} fixed at 1 V. Both the modeled and simulated output characteristics show excellent saturation at high V_{DS}. It may be observed that, despite using non-degenerate doping in the source, the superlinear onset of the output characteristics is not too significant. This is mainly due to the incorporation of the i-Ge region. It has been shown by previous researchers[15] that the superlinear onset in the output characteristics increases with increase in the difference between the longest and the shortest tunnel path lengths. Potential varies linearly with position (x) in the undoped i-Ge region. Thus, incorporation of the i-Ge region in the source helps in improving linearity in the output characteristics by reducing ($L_{max} - L_{min}$). Fig. 6(b) plots the variation of L_{min} and Ψ_S with V_{DS}. The $L_{min} - V_{DS}$ and $\Psi_S - V_{DS}$ characteristics correspond to the modeled output characteristics shown in Fig. 6(a). The $L_{min} - V_{DS}$ characteristic curves decrease gradually up to a certain drain voltage (V_{DSsat}) and then saturate. With V_{GS} fixed at 1 V, as V_{DS} is gradually increased, inversion charges (Q_{inv}) at the i-Ge/gate-oxide interface decrease, leading to an increase in Ψ_S with V_{DS} and corresponding decrease in L_{min}. When V_{DS} is increased beyond V_{DSsat}, Q_{inv} becomes negligible and thus Ψ_S becomes independent of V_{DS}, causing L_{min} saturation beyond V_{DSsat}, as can be observed from the $\Psi_S - V_{DS}$ and $L_{min} - V_{DS}$ characteristics shown in Fig. 6(b). Excellent saturation observed in the device output characteristics can be attributed to the saturation of L_{min} beyond V_{DSsat}.

B. Effect of T_{in} on the device performance

Fig. 7(a) compares the simulated and the modeled transfer characteristics, obtained at the illuminated condition ($\lambda = 0.7\ \mu$m) with V_{DS} fixed at 1 V. T_{in} has been varied in the range of 5 nm to 10 nm, and no gate-to-channel overlap has been considered for this study. The model empirical fitting parameter, N_{OFF}, has been chosen to be $1.5 \times 10^{18}\,\text{cm}^{-3}$. Parameter γ has been varied from (0.82 to 1.05) for $T_{in} = 5$ nm, (0.75 to 1.0) for $T_{in} = 7$ nm, and (0.37 to 0.66) for $T_{in} = 10$ nm, corresponding to λ variation from 0.7 μm to 1 μm. Extracted values of V_{ONSET} and I_{ON} from the simulated transfer characteristics are found to decrease from 0.735 V to 0.677 V, and from 2.14 μA/μm to 1.31 μA/μm, with increase in T_{in}. Modeled transfer characteristics also show a similar trend. As T_{in} increases, potential drop ($\Psi_S - \Psi_B$) across the i-Ge region increases. Consequently, the net source depletion charge decreases. The decrease in V_{ONSET} is due to the reduction in the surface electric field resulting from such decrease in Q_B. The observed trend of decrease in I_{ON} with increase in T_{in} can be understood by inspecting the $L_{min} - \Psi_S$ characteristics, shown in Fig. 7(b). As T_{in} increases, source depletion width increases for a fixed band bending at the i-Ge/gate-oxide interface, which leads to an increase in L_{min}. Such increase in L_{min} reduces the BTBT generation rate and the resultant current. This also results in the decrease of average electric field along the shortest tunnel path. Fig. 8(a) plots the SS - I_{DS} characteristics, extracted from the relevant modeled and simulated input characteristics. The observed deterioration in SS with increase in T_{in} is due to the decrease in the average electric field along the shortest tunnel path. At low current levels in the range of 1 pA/μm to100 pA/μm, good agreement is observed between the SS and I_{DS} characteristics extracted from the simulated and modeled transfer characteristics. In the current range of 100 pA/μm to 10 nA/μm, the modeled transfer characteristic curves exhibit slightly higher SS in comparison to their simulated counterparts. Such deviations are ascribed to the bias dependency of the empirical source doping concentration introduced in Eq. (9), which determines the subthreshold behavior of the modeled transfer characteristics. Thus, the modeled transfer characteristics exhibit higher SS_{AVG} relative to the corresponding simulated transfer characteristics, as can be observed from the plots of variation of SS_{AVG} with λ, shown in Fig. 8(b). Comparative plots of variation of peak spectral sensitivity with T_{in}, corresponding to decrease in λ from (1 μm to 0.9 μm), (0.9 μm to 0.8 μm), and (0.8 μm to 0.7 μm), are shown in Fig. 8(c). S_{nm} values, extracted from the relevant pairs of transfer characteristic curves, obtained from the simulation and model, are observed to decrease, as T_{in} increases, for each wavelength pair considered. Such trends are consistent with the degradation of SS_{AVG} with increase in T_{in}. The S_{nm} values obtained from the model are slightly lesser than those obtained from the simulated transfer characteristics. This is due to the higher SS_{AVG} of the modeled transfer characteristics. Fig. 9(a) compares the simulated and the modeled output characteristics, obtained at the illuminated condition ($\lambda = 0.7\ \mu$m) with V_{GS} fixed at 1 V. Excellent agreement is observed between the simulated and modeled output characteristics. Linearity of the output characteristics is deteriorated with increase in T_{in}. The superlinear onset of the output characteristics is related to the selection of the allowed energy window.[30] As T_{in} increases, drain control over the band bending at the i-Ge/gate-oxide

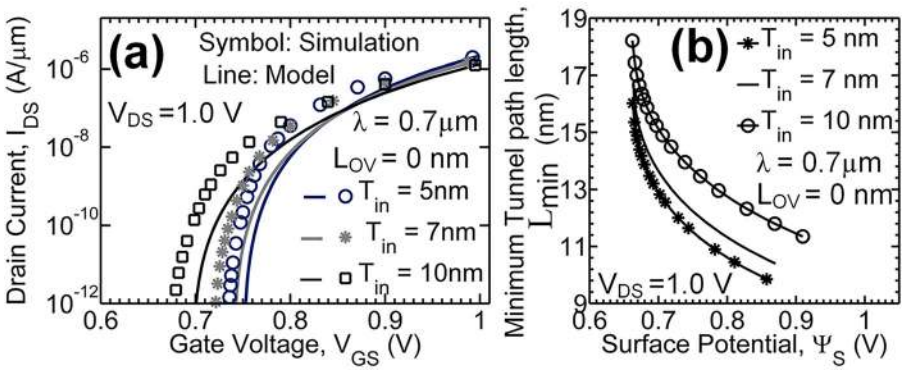

FIG. 7. (a). Comparative plots of input characteristics obtained from the simulation and the model, at the illuminated condition ($\lambda = 0.7\ \mu$m), at $V_{DS} = 1$ V. No gate-to-channel overlap is considered, and T_{in} has been varied in the range of 5 nm to 10 nm. (b) Corresponding $L_{min} - \Psi_S$ characteristics.

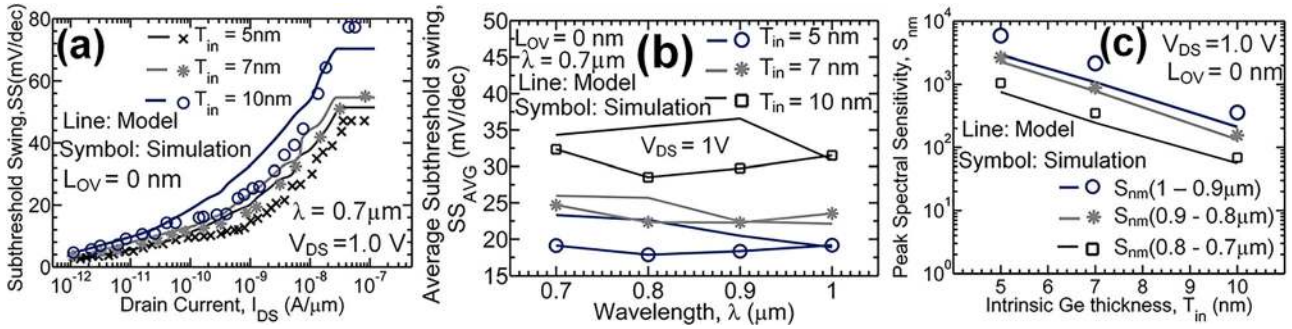

FIG. 8. (a) $SS - I_{DS}$ characteristics extracted from the simulated and modeled input characteristics shown in Fig. 7(a). (b) Comparative plots of variation of SS_{AVG} with λ, extracted from the relevant simulated and modeled transfer characteristics. (c) Plots of variation of S_{nm} with T_{in}, extracted from the relevant pairs of transfer characteristic curves obtained from the simulation and model, corresponding to decrease in λ from (1 μm to 0.9 μm), (0.9 μm to 0.8 μm), and (0.8 μm to 0.7 μm).

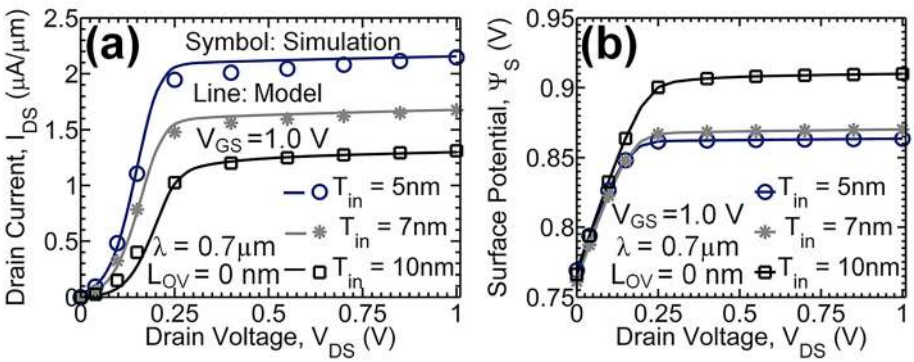

FIG. 9. (a) Comparative plots of output characteristics obtained from the simulation and the model, at the illuminated condition ($\lambda = 0.7\,\mu$m), at $V_{GS} = 1$ V. No gate-to-channel overlap is considered, and T_{in} has been varied in the range of 5 nm to 10 nm. (b) Corresponding $\Psi_S - V_{DS}$ characteristics.

interface increases, as can be observed from the $\Psi_S - V_{DS}$ characteristics shown in Fig. 9(b). These characteristics correspond to the modeled output characteristics. Consequently, at low V_{DS}, the Fermi distribution function (f_{nS}) increases and ($f_{pS} - f_{nS}$) decreases. This results in slower rise in the drain current in the low V_{DS} regime.

C. Effect of gate-to-channel overlap length

Fig. 10(a) plots the simulated input characteristics based on the effect of the gate-to-channel overlap length. Transfer characteristics corresponding to the illumination wavelength of 0.7 μm, obtained at a fixed V_{DS} of 1 V, are shown in Fig. 10(a). T_{in} has been chosen to be 5 nm for this study. It can be observed that, with increase in L_{OV} from 0 nm to 20 nm, V_{ONSET} decreases from 0.735 V to 0.556 V and I_{ON} increases from 2.14 μA/μm to 3.43 μA/μm. Deterioration in the SS can be observed in the corresponding $SS - I_{DS}$ characteristics, shown in Fig. 10(b), with increase in L_{OV}. For explaining such observations, comparative plots of the conduction band profile corresponding to $L_{OV} = 0$ nm and $L_{OV} = 20$ nm are shown in Fig. 11(a). The conduction band profiles are obtained along a cut-line parallel to the gate-oxide interface at a distance of 0.5 nm from it, in the region spanning from: $0 \le y \le (L_D + L_{CH} + L_G)$, with V_{GS} and V_{DS} fixed at 0.7 V and 1 V, respectively. In comparison to the conduction band profile corresponding to $L_{OV} = 0$ nm, greater band bending is observed in the channel region and in the portions of the source region, near to the source-channel junction, in the presence of gate-to-channel overlap. Greater band bending in the channel region enhances the diagonal tunneling component of BTBT current. While, additional band bending in the source region, near to the source-channel junction, caused by the enhanced gate fringing field, increases the BTBT generation due to line tunneling in these regions, as can be observed from the electron BTBT generation rate profile shown in Fig. 11(b). Decrease in V_{ONSET} is mainly due to the decrease in $V_{ONSET}^{diagonal}$ with increase in L_{OV}. The observed trend of increase

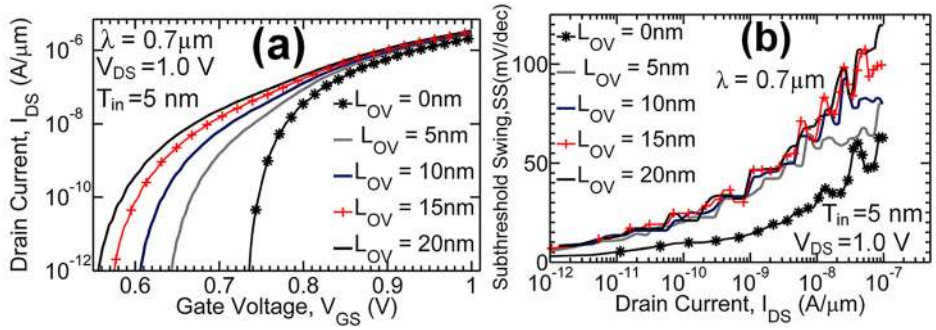

FIG. 10. (a) Simulated input characteristics obtained at the illuminated condition ($\lambda = 0.7\,\mu$m) at $V_{GS} = 1$ V. T_{in} is chosen to be 5 nm, and L_{OV} has been varied in the range of 0 nm to 20 nm. (b) Corresponding $SS - I_{DS}$ characteristics.

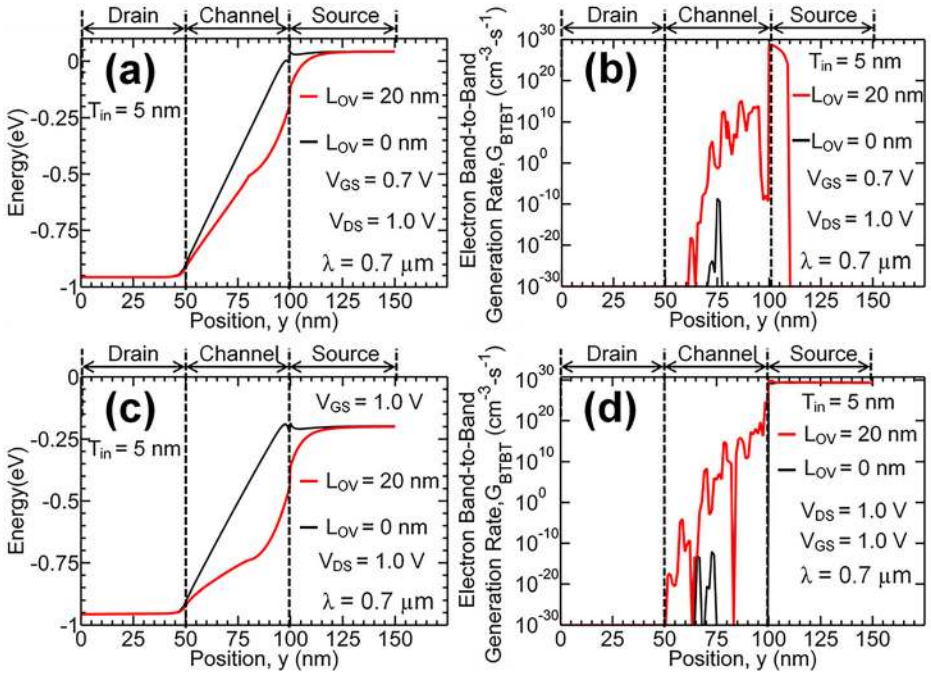

FIG. 11. (a) Comparative conduction band profile along the *y* direction, corresponding to $L_{OV} = 0$ nm and $L_{OV} = 20$ nm, obtained along a cut-line parallel to the gate-oxide interface at a distance of 0.5 nm from it, in the i-Ge region, channel region, and the drain region, with V_{GS} and V_{DS} fixed at 0.7 V and 1 V, respectively. (b) Corresponding electron band-to-band generation rate profile. (c) ON state conduction band profile corresponding to $L_{OV} = 0$ nm and $L_{OV} = 20$ nm. (d) Corresponding electron band-to-band generation rate profile.

in I_{ON} with increase in L_{OV} can be similarly explained from the ON state conduction band profile shown in Fig. 11(c) and the corresponding electron BTBT generation rate profile shown in Fig. 11(d). The increase in I_{ON} with increase in L_{OV} can be ascribed to the increase in the line tunneling component and diagonal tunneling component of BTBT current. Average electric field along a diagonal tunnel path is low. Thus, the dominance of diagonal tunneling reduces the steepness in turn ON of the input characteristics. In the absence of any gate-to-channel overlap, diagonal tunneling is significantly suppressed due to insufficient band bending in the channel region. Consequently, the corresponding input characteristics exhibit very steep *SS*, as can be observed from the $SS - I_{DS}$ characteristics shown in Fig. 10(b). As L_{OV} increases, enhancement in the diagonal tunneling component at low gate voltages causes degradation in *SS*. Thus, SS_{AVG} increases from ∼19 mV/dec to ∼43 mV/dec with increase in L_{OV} from 0 nm to 20 nm, as can be observed from the plots of variation of SS_{AVG} with λ shown in Fig. 12(a). Such degradation in SS_{AVG} causes reduction in the peak spectral sensitivity by almost two orders, as can be observed from the $S_{nm} - L_{OV}$ characteristics shown in Fig. 12(b).

V. CONCLUSION

In this work, a novel optoelectronic TFET has been introduced, which exhibits multi-spectral sensitivity in the wavelength range of 0.7 μm to 1 μm, owing to its steep average subthreshold swing (SS_{AVG}) of ∼19 mV/dec over five current decades. Model predictions of key parameters such as the SS_{AVG}, spectral sensitivity (S_n), and ON current (I_{ON}) have a good match with the TCAD simulation results. The model explains the degradation in spectral sensitivity and linearity of the output characteristics with increase in the thickness of the intrinsic Ge region. TCAD simulation results show that the spectral sensitivity deteriorates with increase in the gate-to-channel overlap length. Noise immunity and the spectral sensitivity of the device can be improved by increasing the electric field along a line tunnel path using higher source doping concentration. However, at very high source doping levels, the onset voltage for line tunneling will increase significantly. This leads to degradation in SS_{AVG} due to dominance of diagonal tunneling and corresponding degradation in spectral sensitivity. Thus, increasing the source doping level will improve the spectral sensing performance of the device as long as line tunneling dominates over diagonal tunneling in the subthreshold regime of device operation.

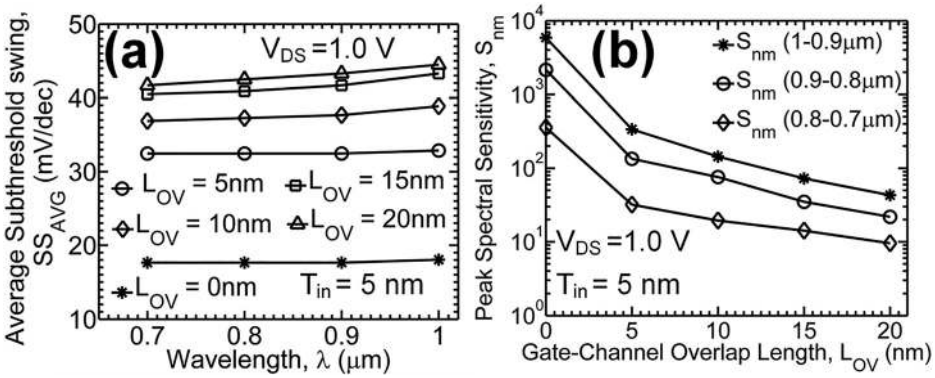

FIG. 12. (a) Plots of variation of SS_{AVG} with λ, extracted from the relevant simulated transfer characteristics. (b) Plots of variation of S_{nm} with L_{OV}, extracted from the relevant pairs of simulated transfer characteristic curves, corresponding to decrease in λ from (1 μm to 0.9 μm), (0.9 μm to 0.8 μm), and (0.8 μm to 0.7 μm).

Thus, the proposed device can be a potential candidate for various near-infrared multi-spectral sensing and imaging applications.

ACKNOWLEDGMENTS

The authors would like to acknowledge the Center of Excellence in System Biology and Biomedical Engineering, Calcutta University, sponsored by TEQIP Phase II, World Bank for providing partial infrastructural support. This work was supported by Department of Electronics and Information Technology, Government of WB, India, under VLSI Design Project. P. S. Gupta gratefully acknowledges Dr. Pradip K. Roy of NexPlanar Corporation for his helpful discussions during the course of this work.

[1]A. Dobroiu, C. Otani, and K. Kawasi, Meas. Sci. Technol. **17**, R161 (2006).
[2]X. Gao, Y. Cui, R. Levenson, L. Chung, and S. Nie, Nat. Biotechnol. **22**, 969 (2004).
[3]L. Yuan, W. Lin, S. Zhao, W. Gao, B. Chen, L. He, and S. Zhu, J. Am. Chem. Soc. **134**, 13510 (2012).
[4]S. Pleasants, Nature Photonics **8**, 351 (2014).
[5]E. Lee, D. Moon, J. H. Yang, K. S. Lim, and Y. K. Choi, IEEE Electron Device Lett. **30**, 493 (2009).
[6]T. Yamagata and K. Shimomura, Jpn. J. Appl. Phys., Part 2 **35**, L1589 (1996).
[7]A. K. Okyay, D. Kuzum, S. Latif, D. A. B. Miller, and K. C. Saraswat, IEEE Trans. Electron Devices **54**, 3252 (2007).
[8]M. Lundstorm and Z. Ren, IEEE Trans. Electron Devices **49**, 133 (2002).
[9]Y. Khatami and K. Banerjee, IEEE Trans. Electron Devices **56**, 2752 (2009).
[10]W. Y. Choi, B.-G. Park, J. D. Lee, and T.-J. K. Liu, IEEE Electron Device Lett. **28**, 743 (2007).
[11]A. M. Ionescu and H. Riel, Nature **479**, 329 (2011).
[12]D. Sarkar and K. Banerjee, Appl. Phys. Lett. **100**, 143108 (2012).
[13]N. Dagtekin and A. M. Ionescu, Appl. Phys. Lett. **105**, 232105 (2014).
[14]P. S. Gupta, S. Chattopadhyay, P. Dasgupta, and H. Rahaman, IEEE Trans. Electron Devices **62**, 1516 (2015).
[15]S. Verhulst, D. Leonelli, R. Rooyackers, and G. Groeseneken, J. Appl. Phys. **110**, 024510 (2011).
[16]Sentaurus Device User Guide, version G-2012.06 (2012).
[17]W. Hsu, J. Mantey, L. F. Register, and S. K. Banerjee, IEEE Trans. Electron Devices **62**, 2292 (2015).
[18]A. M. Walke, W. G. Vandenberghe, K-H. Kao, A. Vandooren, and G. Groeseneken, IEEE Trans. Electron Devices **60**, 1019 (2013).
[19]W. G. Vandenberghe, B. Soree, W. Magnus, G. Groeseneken, and M. V. Fischetti, Appl. Phys. Lett. **98**, 143503 (2011).
[20]E. O. Kane, J. Appl. Phys. **32**, 83 (1961).
[21]P. Chakrabarti, N. L. Shrestha, S. Srivastava, and V. Khemka, IEEE Trans. Electron Devices. **39**, 2050 (1992).
[22]L. J. A. Koster, V. D. Mihailetchi, R. Ramaker, and P. W. M. Blom, Appl. Phys. Lett. **86**, 123509 (2005).
[23]S. Persson, P.-E. Hellberg, and S.-L. Zhang, Solid-State Electron. **46**, 2209 (2002).
[24]G. A. M. Hurkx, D. B. M. Klaassen, and M. P. G. Knuvers, IEEE Trans. Electron Devices **39**, 331 (1992).
[25]S. H. Kim, S. Agarwal, Z. A. Jacobson, P. Matheu, C. Hu, and T.-J. K. Liu, IEEE Electron Device Lett. **31**, 1107 (2010).
[26]D. E. Aspnes and J. B. Theeten, J. Electrochem. Soc. **127**, 1359 (1980).
[27]J. T. Smith, C. Sandow, S. Das, R. A. Minamisawa, S. Mantl, and J. Appenzeller, IEEE Trans. Electron Devices **58**, 1822 (2011).
[28]A. Florakis, N. Misra, C. Grigoropoulos, K. Giannakopoulos, A. Halimaoui, and D. Tsoukalas, Mater. Sci. Eng. B **154/155**, 39 (2008).
[29]G. Han, Y. S. Yee, P. Guo, Y. Yang, L. Fan, C. Zhan, and Y-C. Yeo, in *Silicon Nanoelectronics Workshop* (*SNW*), *Kyoto*, Japan (IEEE, 2011), pp. 1–2.
[30]P.-Y. Wang and B.-Y. Tsui, IEEE Trans. Nanotechnol. **15**, 74 (2016).